PHYSICAL REVIEW C **76**, 014004 (2007)

# Differential cross section and analyzing power measurements for $\vec{n}d$ elastic scattering at 248 MeV

Y. Maeda,[1,*] H. Sakai,[2,3] K. Fujita,[4] M. B. Greenfield,[5] K. Hatanaka,[4] M. Hatano,[2] J. Kamiya,[6] T. Kawabata,[1] H. Kuboki,[2] H. Okamura,[4] J. Rapaport,[7] T. Saito,[2] Y. Sakemi,[4,†] M. Sasano,[2] K. Sekiguchi,[3] Y. Shimizu,[4,‡] K. Suda,[1,§] Y. Tameshige,[4] A. Tamii,[4] T. Wakasa,[8] K. Yako,[2] J. Blomgren,[9] P. Mermod,[9] A. Öhrn,[9] M. Österlund,[9] H. Witała,[10] A. Deltuva,[11] A. C. Fonseca,[11] P. U. Sauer,[12] W. Glöckle,[13] J. Golak,[10] H. Kamada,[14] A. Nogga,[15] and R. Skibiński[10]

[1]*Center for Nuclear Study, The University of Tokyo, Bunkyo, Tokyo 113-0033, Japan*
[2]*Department of Physics, The University of Tokyo, Bunkyo, Tokyo 113-0033, Japan*
[3]*RIKEN, Institute of Physical and Chemical Research, Wako Saitama 351-0198, Japan*
[4]*Research Center for Nuclear Physics, Osaka University, Ibaraki, Osaka 567–0047, Japan*
[5]*International Christian University, Mitaka, Tokyo 181-8585, Japan*
[6]*Japan Atomic Energy Agency, Tokai, Ibaraki 319-1195, Japan*
[7]*Department of Physics, Ohio University, Athens, Ohio 45701, USA*
[8]*Department of Physics, Kyushu University, Higashi, Fukuoka 812-8581, Japan*
[9]*Department of Neutron Research, Uppsala University, S-75120 Uppsala, Sweden*
[10]*Institute of Physics, Jagiellonian University, PL-30059 Cracow, Poland*
[11]*Centro de Física Nuclear da Universidade de Lisboa, P-1649-003 Lisboa, Portugal*
[12]*Institut für Theoretische Physik, Universität Hannover, D-30167 Hannover, Germany*
[13]*Institut für Theoretische Physik II, Ruhr-Universität Bochum, D-44780 Bochum, Germany*
[14]*Department of Physics, Faculty of Engineering, Kyushu Institute of Technology, Kitakyushu 804-8550, Japan*
[15]*Institut für Kernphysik, Forschumgszentrum Jülich, D-52425 Jülich, Germany*

(Received 13 November 2006; published 19 July 2007)

The differential cross sections and vector analyzing powers for $nd$ elastic scattering at $E_n = 248$ MeV were measured for $10^\circ$–$180^\circ$ in the center-of-mass (c.m.) system. To cover the wide angular range, the experiments were performed separately by using two different setups for forward and backward angles. The data are compared with theoretical results based on Faddeev calculations with realistic nucleon-nucleon ($NN$) forces such as AV18, CD Bonn, and Nijmegen I and II, and their combinations with the three-nucleon forces (3NFs), such as Tucson-Melbourne 99 (TM99), Urbana IX, and the coupled-channel potential with $\Delta$-isobar excitation. Large discrepancies are found between the experimental cross sections and theory with only $2N$ forces for $\theta_{\mathrm{c.m.}} > 90^\circ$. The inclusion of 3NFs brings the theoretical cross sections closer to the data but only partially explains this discrepancy. For the analyzing power, no significant improvement is found when 3NFs are included. Relativistic corrections are shown to be small for both the cross sections and the analyzing powers at this energy. For the cross sections, these effects are mostly seen in the very backward angles. Compared with the $pd$ cross section data, quite significant differences are observed at all scattering angles that cannot be explained only by the Coulomb interaction, which is usually significant at small angles.

DOI: 10.1103/PhysRevC.76.014004 PACS number(s): 21.30.−x, 21.45.+v, 24.10.Jv, 25.40.Dn

## I. INTRODUCTION

Studies of few-nucleon systems allow us to test current models of nuclear forces through comparisons of precise data and rigorous theoretical predictions. Modern $NN$ potentials, such as AV18 [1], CD Bonn [2], and Nijmegen I, II, and 93 [3], very accurately reproduce a rich set of experimental $NN$ data up to a laboratory energy of 350 MeV. These realistic $NN$ interactions are, at least partially, based on the traditional meson-exchange picture.

When applied to many-body ($>2N$) systems, the $NN$ potentials fail to predict experimental binding energies. Theoretical predictions underestimate binding energies by 0.5–1 MeV for $^3$H and $^3$He and by 2–4 MeV for $^4$He [4,5]. For heavier nuclei, disagreements become larger as demonstrated by calculations using stochastic techniques [6,7]. These results indicate the necessity of the introduction of many-body interactions. The three-nucleon force (3NF) is considered to be the most important among them. Present-day 3NF models, such as the Tucson-Melbourne (TM) [8] and the Urbana IX 3NF [9], are mostly based on $2\pi$ exchange between three nucleons with the intermediate $\Delta$-isobar excitation [10]. These forces can provide additional binding when included in the nuclear Hamiltonian. Taking appropriate parameters, one can reproduce the correct binding energies of $3N$ and $4N$ systems [4,5]. Addition of the 3NF drastically improves the description

---

[*] Department of Physics, Kyushu University, Higashi, Fukuoka 812-8581, Japan; yukie@kutl.kyushu-u.ac.jp

[†] Cyclotron and Radioisotope Center, Tohoku University, Sendai, Miyagi 980-8578, JAPAN

[‡] Center for Nuclear Study, The University of Tokyo, Bunkyo, Tokyo 113-0033, Japan

[§] Research Center for Nuclear Physics, Osaka University, Ibaraki, Osaka 567-0047, Japan

of low energy bound states of up to $A = 10$ nuclei [7]. On the other hand, nuclear forces recently derived from chiral perturbation theory ($\chi$PT) have become available for laboratory energies below 100 MeV and lead to a comparable reproduction of the $2N$ data set [11–13]. The $\chi$PT approach is expected to give more systematic understanding of nuclear forces than the traditional approach.

Elucidation of the properties of 3NFs is one of the principal topics in nuclear physics. Nucleon-deuteron (*Nd*) scattering is expected to be a good probe for a detailed investigation of 3NFs. Cross sections [14–20] and spin observables, such as analyzing powers [21–24], spin correlation coefficients [25], and polarization transfer coefficients [26,27] have been measured for elastic *Nd* scattering. Large discrepancies between these data and theoretical predictions based on exact solutions of the Faddeev equations with only modern *NN* forces are reported. These discrepancies are particularly significant in the angular region of the cross section minima and at energies of incoming nucleons above about 60 MeV [28]. However, concerning the differential cross sections and vector analyzing powers, the inclusion of the $2\pi$-exchange 3NF models such as TM-3NF or Urbana IX-3NF into the calculations removes many of the discrepancies. This result clearly shows 3NF effects in the $3N$ continuum and forms a basis to test new theoretical 3NF force models. In contrast, theoretical calculations with 3NFs still have difficulties in reproducing data of some spin observables.

In Ref. [27], the precise data for the cross section and spin transfer coefficients of the $^2\mathrm{H}(\vec{p}, \vec{p})^2\mathrm{H}$ reaction at 250 MeV are reported. The large discrepancies between cross section data and theoretical calculations based on *NN* forces are only partially removed by including 3NFs. This contrasts with the case of 135 MeV *pd* elastic scattering reported in Ref. [18] where inclusion of 3NFs leads to good agreement between data and calculations. This implies that at higher energies, not only spin observables but also cross sections indicate the deficiencies of the present 3NF models. The energy dependence of the discrepancies found in Ref. [27] is similar to that observed in the total *nd* cross section [29,30] where inclusion of 3NFs only partially improves the agreement with the data at higher energies. In Ref. [30], it is indicated that at higher energies, corrections to the *nd* total cross section resulting from relativistic kinematics are comparable in magnitude to the effects of 3NF. An estimation of the magnitude of relativistic effects is required before coming to any conclusion regarding the origin of the remaining discrepancy for the cross section at 250 MeV.

In *pd* reactions, in addition to nuclear forces, the Coulomb interaction between two protons is present. Despite recent efforts to introduce the Coulomb interaction in the calculations of elastic *pd* scattering [31–34], no results were available for energies as high as 250 MeV until quite recently [35,36]. A direct comparison of *nd* and *pd* data is the simplest form for studying the importance of Coulomb effects in the three-nucleon system. To study the 3NF forces in the absence of the Coulomb interaction, we measured the $^2\mathrm{H}(\vec{n}, n)^2\mathrm{H}$ elastic reaction using a 248 MeV polarized neutron beam at the Research Center for Nuclear Physics (RCNP) of Osaka University. The cross sections and analyzing powers were measured over a wide angular range $\theta_{\mathrm{c.m.}} = 10°$–$180°$. To cover such a wide angular range, we applied two methods: detection of recoiled deuterons via a magnetic spectrometer for the backward angles, and detection of scattered neutrons via a time of flight (TOF) method for the forward angles.

The experimental details are presented in Secs. II and III. In Sec. IV we briefly describe the basics of $3N$ scattering theory and how relativistic corrections are incorporated into the Faddeev calculations. The data are compared with the theoretical predictions in Sec. V, and conclusions are given in Sec. VI.

## II. EXPERIMENTAL PROCEDURE FOR BACKWARD SCATTERING

The measurements in the backward angular region ($\theta_{\mathrm{c.m.}} \geqslant 60°$) were carried out at the $(n, p)$ facility [37] constructed in the west RCNP experimental hall. The neutron beam was produced by the $^7\mathrm{Li}(\vec{p}, \vec{n})^7\mathrm{Be}$ reaction, and it subsequently bombarded the deuteron targets. The recoiled charged particles were momentum analyzed by the large acceptance spectrometer (LAS). The elastic $^1\mathrm{H}(\vec{n}, p)n$ reaction was measured to calibrate the intensity of the neutron beam as well as the acceptance of the LAS.

### A. Polarized neutron beam

The polarized proton beam was provided by the high-intensity polarized ion source (HIPIS) [38]. The beam was extracted from HIPIS and injected into the Azimuthally Varying Field (AVF) cyclotron. The radio frequency (RF) of the AVF cyclotron was 14.496 MHz with a beam-pulse period of 69.0 ns. The preaccelerated proton beam was accelerated in the Ring cyclotron up to 250 MeV. The beam was single-turn extracted and transported to the $(n, p)$ facility through the WS course [39].

The beam polarization was monitored continuously by two beamline polarimeters BLP1 and BLP2 placed in the beamline. The beam polarization was measured using the $^1\mathrm{H}(\vec{p}, p)^1\mathrm{H}$ reaction [40]. Both polarimeters used polyethylene films as hydrogen targets. The scattered and recoiled protons were detected in coincidence by a pair of plastic scintillators placed at $\theta_{\mathrm{lab}} = 17.0°$ and $70.9°$. Four sets of detectors were placed in left, right, up, and down directions.

The asymmetry measured by the polarimeters contains contributions of the quasi-elastic $(\vec{p}, p)$ reaction from the carbon nucleus. The analyzing power for this reaction is different from the analyzing power of the free *pp* scattering. The effective analyzing power of the polarimeter, including hydrogen and carbon contributions at a proton energy of 250 MeV at $\theta_{\mathrm{lab}} = 17.0°$, was measured to be $A_y = 0.362 \pm 0.003$ [27]. A typical value of the proton polarization was 0.6 during this experiment.

Figure 1 shows the schematic view of the $(n, p)$ facility. The primary proton beam was achromatically transported to a $^7\mathrm{Li}$ target mounted in a neutron production chamber. This chamber was placed in between the pole gap of the C-shape clearing magnet [41] which was inclined by 24.05° with respect to the vertical axis, allowing the proton beam to be deflected to the beam dump in the floor.

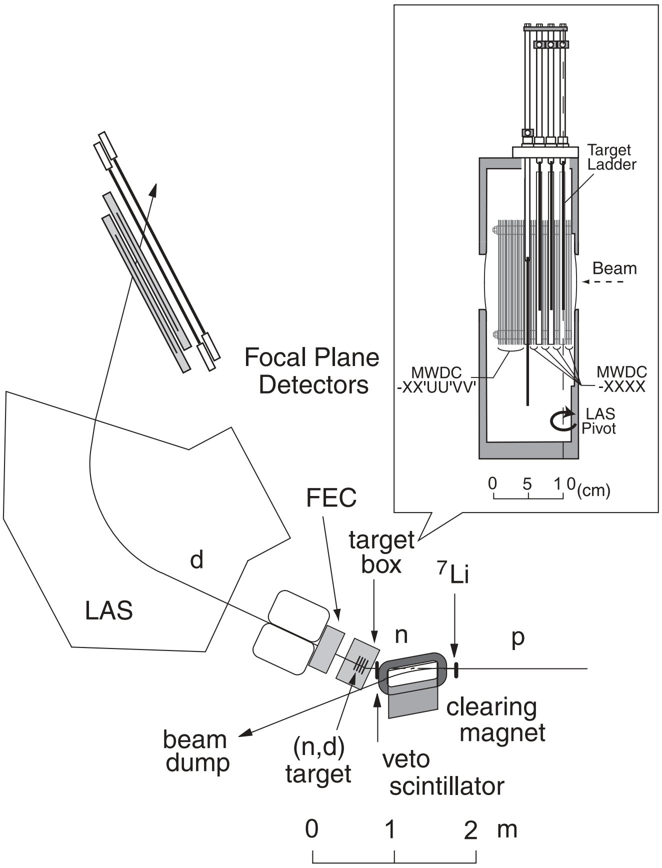

FIG. 1. Schematic view of ($n$, $p$) facility at RCNP. This facility mainly consists of a vacuum chamber for the neutron beam production, a clearing magnet for sweeping the primary beam, and a segmented target system with two MWDC boxes. The recoiled charged particles are momentum analyzed by the LAS and detected at the focal plane.

The “quasi-mono-energetic” polarized neutron beam was produced by the $^7\mathrm{Li}(\vec{p}, n)^7\mathrm{Be}$ reaction in the vacuum chamber. We selected the produced neutrons corresponding to the transitions to both the ground state and the first excited state at 0.43 MeV in $^7$Be. The energy and spread of the neutron beam were 248 MeV and 2 MeV full width at half maximum (FWHM), respectively.

The produced neutron beam traverses the clearing magnet and passes through the vacuum window of a 10 $\mu$m-thick aramid film at the end of the vacuum chamber. The neutrons further pass through a veto counter made of 1-mm-thick plastic scintillator with a size of $40^W \times 34^H$ cm$^2$ which was positioned just downstream of the vacuum chamber. Signals from this counter are used to reject the events regarded as due to charged particles. The typical count rate of this veto counter is 400 kHz when a 250 nA proton beam bombards a $^7$Li target with a 560 mg/cm$^2$ thickness.

The differential cross section and polarization transfer coefficient for the $^7\mathrm{Li}(\vec{p}, n)$ reaction at 0° are $\frac{d\sigma}{d\Omega}_{\mathrm{lab}} = 37.4 \pm 1.1$ mb/sr [42] and $D_{NN} = -0.28 \pm 0.05$ [43], respectively. Thus the typical intensity and polarization of the resulting neutron beam over the deuteron target area of $30^W \times 20^H$ mm$^2$ were estimated to be $2 \times 10^6$/s and $P_n = 0.2$, respectively.

### B. Targets

The ($n$, $p$) facility is equipped with a segmented target system. The advantage of such a target system is the use of several targets, thus increasing the total target thickness while maintaining good angular resolution, yet without sacrificing energy resolution. General features of the target system are similar to those developed at TRIUMF [44]. In the present setup, we used two multiwire drift chamber (MWDC) boxes, called the target box and the front-end chamber (FEC) box, between the clearing magnet and the LAS. The target box has ten wire planes ($X_1$-$X_2$-$X_3$-$X_4$-$XX'UU'VV'$) and the FEC box has six wire planes ($YY'VV'UU'$).

The target box has four target ladders. Each target ladder is positioned behind four $X_i$-wire planes. Because the MWDC planes are only sensitive to charged particles, the specific target from which the recoiling particle is emitted can be identified, thus making it possible to correct for the energy loss of recoiled particles in the downstream targets. For deuteron targets, we used four films of self-supporting deuterated polyethylene ($\mathrm{C^2H_2}$, denoted in the following as $\mathrm{CD_2}$) [45] with thicknesses of 100–220 mg/cm$^2$. In addition to deuteron targets, we used polyethylene ($\mathrm{CH_2}$) films with thicknesses of 90–190 mg/cm$^2$ as proton targets for the $np$ measurements. Graphite targets were also employed for the purpose of carbon background subtraction.

The trajectory of the outgoing particles were measured with six wire planes ($XX'UU'$VV$'$) in the target box and by the FEC. Both MWDC boxes are rotated around the LAS pivot according to the setting angle of LAS. Thus, the various target areas presented to the neutron beam depended upon the LAS setting.

A gas mixture of argon (50%) and ethane (50%) was used for the counter gas. For the $np$ measurements, hydrogen in the chamber gas could be a source of background. However, the hydrogen content of the gas was less than 1% of that in the polyethylene targets, so the uncertainty in the data caused by hydrogen contamination is smaller than the systematic uncertainty of the target thickness.

### C. Measurements

The recoil deuterons or protons were momentum analyzed by LAS [46], which has a large momentum bite of $p_{\max} = 1.3 p_{\min}$ with an angular acceptance of 20 msr. Such a large acceptance allows us to cover the angular range of $\Delta\theta_{\mathrm{lab}} = \pm 3.5^\circ$ in one setting. It also covers an effective target size of $30^W \times 20^H$ mm$^2$. The intrinsic energy resolution of LAS is better than $\Delta E = 100$ keV for 250 MeV protons.

The focal plane detectors consisted of a pair of vertical drift chambers (VDC) [47] and two planes of $\Delta E$ plastic scintillation counters. Each VDC consisted of wire planes with the $XU$ configuration.

### D. Data reduction

Data reduction included particle identification, ray tracing, and background subtraction. First of all, the outgoing deuterons (protons) were identified by using the particle TOF

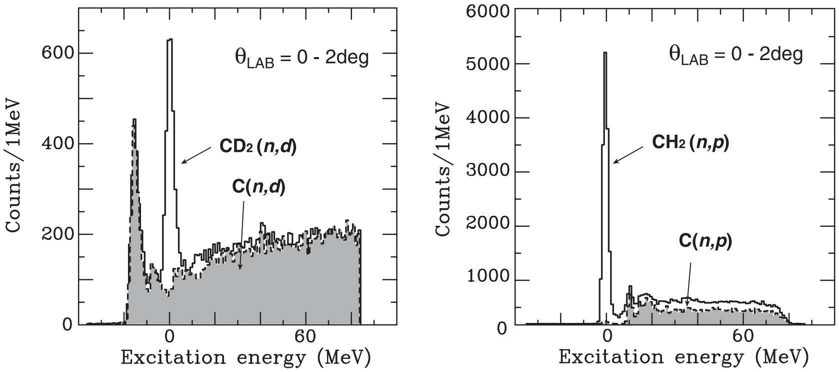

FIG. 2. Solid lines in left and right panels show the spectra of $CD_2(n,d)$ and $CH_2(n,p)$, respectively. Shaded spectra were obtained from measurements with graphite targets. By subtracting the spectra of graphite targets from those of $CD_2$ and $CH_2$, we obtained the spectra of *nd* and *np* elastic scattering.

through the spectrometer and the charge information in the plastic scintillation counters at the focal plane. The protons and deuterons were clearly distinguished from each other. The energy of the recoiled particle was obtained by using the ion optical matrix of the LAS. The information from MWDCs of the target system was used to correct for the energy loss in targets and deduce the reaction angle. Figure 2 shows the spectra obtained with $CD_2$ (left side) and $CH_2$ (right side) targets. In the figure, the spectra obtained with graphite targets are also shown by shaded area. Normalization factors were determined from target thicknesses and beam charges without additional parameters. By subtracting the normalized spectrum of the graphite target from that of the $CD_2$ or $CH_2$ target, we obtained the yields of the *nd* and *np* elastic scatterings, respectively.

## III. EXPERIMENTAL PROCEDURE FOR FORWARD SCATTERING

The measurements for the forward angle region ($\theta_{\text{c.m.}} \leqslant 60^\circ$) were carried out at the RCNP neutron time-of-flight (NTOF) facility [48]. The neutron beam, produced by the $^7\text{Li}(p,n)^7\text{Be}$ reaction, bombarded a deuteron target. Energies of the scattered neutrons were determined via TOF, with neutron detectors located at a 70 m flight path. A deuterated liquid scintillator target (LST) was used as the deuteron target and coincidence measurements of neutrons and deuterons were performed.

### A. Polarized neutron beam

The polarized proton beam was accelerated to 250 MeV by the Ring cyclotron and transported to the N0 experimental hall. The beam pulsing device, which is installed in the injection line between the AVF and the Ring cyclotrons, was used to reduce the wraparound of slow neutrons from preceding beam pulses. In the present study, one of every three beam pulses was used, resulting in a beam pulse interval of 207 ns.

The beam polarization was monitored by a beamline polarimeter (BLP) placed in the beamline between the Ring cyclotron and the N0 experimental hall. The polarimetry of the BLP is the same as that described in Sec. II A.

Figure 3 shows a schematic view of the NTOF facility. The primary proton beam was transported to the $^7\text{Li}$ target within a vacuum chamber and then swept into the beam dump in the wall by the swinger magnet. The energy of the neutrons thus produced was 248 MeV with a spread of 2 MeV FWHM. The vacuum chamber has an exit window of polyethylene with a thickness of 1 mm. The produced neutrons passed through the window and bombarded the deuteron target. The active deuteron target was located 2 m downstream from the $^7\text{Li}$ target at an angle of 0° with respect to the incident proton beam. The scattering angle of the $^2\text{H}(n,n)$ reaction was varied between $\theta_{\text{lab}} = 0^\circ$–$38^\circ$ ($\theta_{\text{c.m.}} = 0^\circ$–$60^\circ$) by moving the positions of the $^7\text{Li}$ target along the proton beam trajectory and adjusting the positions of the deuteron target accordingly. The neutron detector position was fixed in the TOF tunnel at a distance of 70 m from the $^7\text{Li}$ target for all scattering angles.

### B. Targets

A deuterated liquid scintillator BC537 was used as an active deuteron target. Coincidence measurements of neutrons and protons were performed to reduce background events. The liquid target was contained in a 1 mm thick aluminum cylinder with a diameter of 9 cm and length of 6 cm. This container had a window of hard glass (Pyrex) to which a photomultiplier tube (PMT) was attached through a light guide. A booster circuit was installed in the base of the PMT to compensate for the reduction in gain during high counting rates. The inside of the container was coated with $MgO_2$ reflecting paint. A reservoir tube was connected to the container to absorb the expanded volume of the liquid scintillator.

A veto counter of a $70^W \times 90^H \times 0.1^t$ cm$^3$ plastic scintillator was positioned 10 c.m. upstream of the active target. Signals from this counter were used to reject events due to charged particles.

To remove background events originating from $\gamma$ rays, we introduced neutron-gamma ($n\gamma$) discrimination, which is based upon the difference between the pulse shapes for the different type of radiations. To distinguish the different pulse shapes, the integrated charge from two analog-to-digital converter (ADC) gates with different integration times were obtained for each event. One gate covered the peak region of the light pulse and had a width of 100 ns (peak ADC), and the other corresponded to the tail component and had a width of 350 ns (tail ADC).

The *np* elastic scattering using an NE213 liquid scintillator as the proton target was measured for the purpose of normalization.

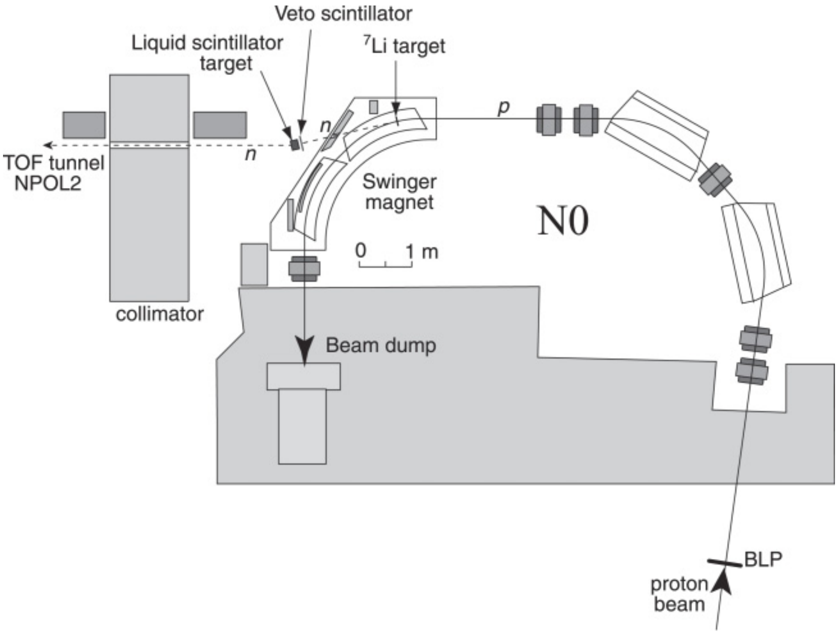

FIG. 3. Schematic layout of neutron time-of-flight (NTOF) facility at RCNP. This facility mainly consists of a swinger magnet, thick collimator wall, 100 m TOF tunnel, and neutron detector NPOL II. Scattered neutrons and the recoiled deuterons are detected by the NPOL II and the active deuteron target, respectively.

### C. Measurements

The scattered neutrons traversed the 70 m flight path in the TOF tunnel and were subsequently detected by the neutron detector NPOL II [49]. It consists of six planes of two-dimensionally position-sensitive neutron detectors. The upstream four planes are BC519 liquid scintillator counters with dimensions of $1^H \times 1^W \times 0.1^t$ m$^3$, and the other two planes are BC408 plastic scintillator counters with the same dimensions. A PMT was attached to each corner (left-up, left-down, right-up, right-down). Three sets (left, middle, right) of thin plastic scintillators with a size of $102^H \times 35^W \times 0.5^t$ cm$^3$, placed in front of each neutron detector, distinguished neutrons from charged particles. Pairs of PMTs and light guides were attached to the tops and bottoms of these plastic counters. The neutron detection efficiency was determined from the measurement for the $^7$Li$(p,n)^7$Be(g.s.+0.43 MeV) reaction, which is known to have an almost constant center-of-mass cross section of $\sigma_{\text{c.m.}}(0^\circ) = 27.0 \pm 0.8$ mb/sr over a wide energy range [42]. The total efficiency for the six planes of neutron detectors was measured to be $25.0 \pm 0.8\%$ when the threshold level of the light output was set to 5 MeV$_{ee}$. The energy of the detected neutron was determined by its TOF, defined as the calibrated time difference between the neutron trigger and RF signal.

### D. Data reduction

Data reduction included determination of the neutron TOF, particle identification in the active targets, and background subtractions.

Scattered neutrons were identified at the NPOL II, the energies of which were determined from their calibrated TOF. In addition, events originating from the neutron beam were selected by applying the $n\gamma$ discrimination method to the active targets. To discriminate neutron events from $\gamma$ events, we calculated the ratio of peak-ADC to tail-ADC as

$$\text{ADC}_{\text{ratio}} = (\text{ADC}_{\text{tail}} - \alpha)/\text{ADC}_{\text{peak}}, \tag{1}$$

where the constant $\alpha$ was determined empirically. The correlation between peak-ADC and the ADC ratio as well as the gate applied for selection of valid neutron events is illustrated in the left panel of Fig. 4. Most $\gamma$ rays and background neutrons were rejected. In that case, the events of neutron elastic or inelastic scattering at low excitation energy from the carbons in the active target did not contribute to the true coincidence events, because the energies of recoiled carbons were smaller enough than that of recoiled deuterons. Remaining background events and the contribution from carbons were removed by subtracting the accidental coincident events. The timing information of the liquid scintillator target was used in this process. The middle and right panels of Fig. 4 show the energy spectra of $nd$ and $np$ elastic scattering, respectively, including the accidental backgrounds (white histogram) and that of the accidental backgrounds only (gray histogram). By subtracting the spectrum of accidental events, yields of the elastic scattering peak were obtained.

## IV. THEORETICAL FORMALISM

The energy of this work is just above the pion production threshold at 215 MeV. Realistic $NN$ potentials have been obtained by analyzing the $NN$ database up to 350 MeV, corresponding to the same center-of-mass energy as 259 MeV in the $nd$ system. All formalisms dealt with in this section do not include pion production, the use of which with the $NN$ potentials is still acceptable at 250 MeV.

### A. Formulation with 3NFs

The breakup operator $T$ of the $3N$ system, in which nucleons interact through the $NN$ potential $V$ and the $3N$ force $V_4$, obeys the equation [50,51]

$$\begin{aligned} T &= tP + (1 + tG_0)V_4^{(1)}(1 + P) + tPG_0T \\ &\quad + (1 + tG_0)V_4^{(1)}(1 + P)G_0T\,. \end{aligned} \tag{2}$$

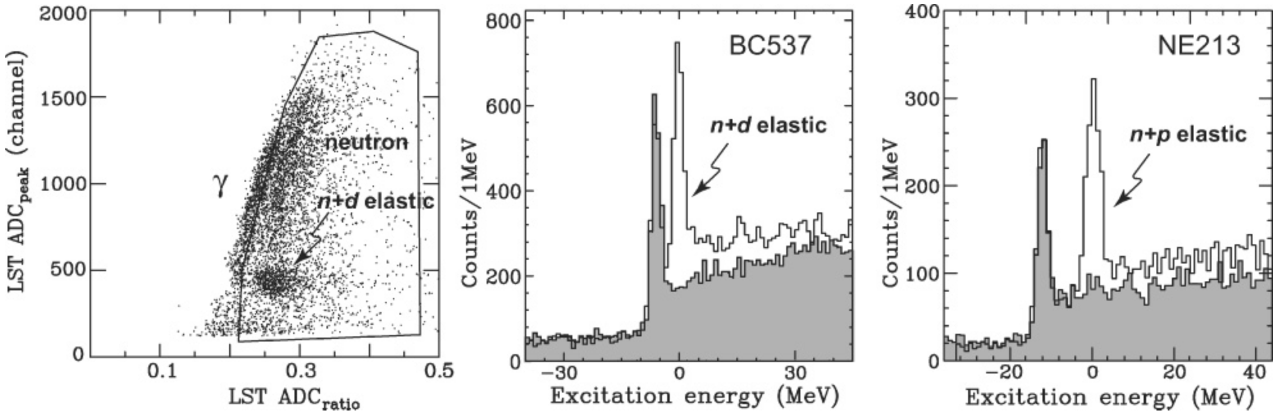

FIG. 4. Left panel shows the discrimination of neutron beam events from $\gamma$ beam events; cluster of *nd* elastic events can be seen. Middle and right panels show the spectra at $\theta_{\text{lab}} = 13^\circ$ obtained with the BC537 and NE213 scintillators. White and gray histograms represent the energy excitation spectra corresponding to true coincidences and accidental coincidences, respectively.

Here $t$ is the two-body t-matrix resulting from $V$ through the Lippmann-Schwinger equation. The potential $V_4^{(1)}$ is symmetric under exchange of nucleons 2 and 3. Together with $V_4^{(2)}$ and $V_4^{(3)}$ they sum up to $V_4$. The quantity $G_0$ is the free $3N$ propagator and the permutation operator $P = P_{12}P_{23}+P_{13}P_{23}$, where $P_{ij}$ interchanges nucleons $i$ and $j$. By use of $T$, the elastic scattering cross section is obtained from the elastic scattering transition matrix element $\langle\phi'|U|\phi\rangle$

$$\begin{aligned}\langle\phi'|U|\phi\rangle &= \langle\phi'|PG_0^{-1} + V_4^{(1)}(1+P) + PT \\ &\quad + V_4^{(1)}(1+P)G_0T|\phi\rangle\,. \end{aligned} \tag{3}$$

The initial state $|\phi\rangle = |\vec{q}_0\rangle|\phi_d\rangle$ is composed of a deuteron wave function $|\phi_d\rangle$ and a momentum eigenstate of the nucleon-deuteron motion with relative momentum $\vec{q}_0$. In the outgoing state $|\phi'\rangle$, the direction of this momentum is changed.

Currently Eq. (2) is solved numerically using a momentum space partial-wave basis. In order to achieve convergence at 250 MeV, all partial-wave states with total angular momenta in the $2N$ subsystem up to $j = 5$ were used, and all total angular momenta in the $3N$ system up to $J = 25/2$ were taken into account. For a shorter range 3NF, inclusion of up to $J = 13/2$ was sufficient. The details of the formalism and the numerical performance are given in Refs. [50–53]. We use the modern $2N$ potentials AV18, CD Bonn, and Nijmegen I and II, and combine them with the TM99 3NF [54] taking the cutoff values $\Lambda = 4.764$, 4.469, 4.690, and 4.704 in units of $m_\pi$, respectively. These $\Lambda$ values were determined for each $NN$ potential so as to reproduce the $^3$H binding energy under combination with the TM99 3NF. The TM99 is a recent version of the TM force which is more consistent with chiral symmetry [55,56]. We also combine the AV18 potential with the Urbana IX 3NF.

### B. Formulation with explicit Δ-isobar excitation

An alternative theoretical description is given in the framework employed in Ref. [57]. The dynamics is based on the charge-dependent CD Bonn potential [58] and its coupled-channel extension allowing for the single excitation of a nucleon to a Δ isobar [59]. That extension, called CD Bonn + Δ, provides a high-quality fit to the two-nucleon data as is the case for the CD Bonn potential. The Δ isobar mediates an effective 3NF in the three-nucleon system besides other Δ-isobar effects. Prominent contributions are of the Fujita-Miyazawa type [10] and of the Illinois ring type [7]. The contributions are based on all meson exchanges, i.e., $\pi$, $\rho$, $\sigma$, and $\omega$ exchanges, contained in the coupled-channel potential. Thus, the arising effective 3NF is much richer with respect to Δ excitation and also has shorter range components than standard irreducible $2\pi$-exchange 3NFs. However, an irreducible 3NF covering other physics mechanisms is not used.

The elastic scattering transition matrix $U$ is obtained from the symmetrized Alt-Grassberger-Sandhas equation [60]

$$U = PG_0^{-1} + PtG_0U, \tag{4}$$

which, when irreducible 3NFs are neglected, is equivalent to Eqs. (2) and (3). Equation (4) is solved in momentum space using a partial-wave expansion. The two-baryon interaction up to total angular momentum of $j = 8$ is taken into account, and three-particle partial waves up to total angular momentum $J = 35/2$ are included. In the case of *pd* scattering, the above technique is extended as described in Refs. [35,61] to include the Coulomb interaction between the charged baryons.

### C. Relativistic formalism

In view of the relatively large incident energy of the present *nd* system, we have also studied the effects of relativity on the elastic scattering cross section and vector analyzing power. This is done assuming that only $2N$ forces are acting. We follow the formalism of Ref. [62] to treat the relativistic three-body Faddeev equations with a boosted two-nucleon potential $V$ expressed in terms of the relativistic potential $v$ given in the $2N$ c.m. system as

$$V(\vec{p}) \equiv \sqrt{[\omega(\vec{k}) + v]^2 + \vec{p}^{\,2}} - \sqrt{\omega(\vec{k})^2 + \vec{p}^{\,2}}\,. \tag{5}$$

The momentum $\vec{p}$ is the total momentum of the two-nucleon system, $\vec{k}$ and $-\vec{k}$ are the individual momenta of the nucleons in their $2N$ c.m. system, and $\omega(\vec{k}) \equiv 2\sqrt{\vec{k}^2 + m^2}$ is the $2N$ free mass operator. We do not treat the boosted potential matrix element in all its complexity [63] but restrict it only to the leading order in $p/\omega$ expansion

$$V(\vec{k}, \vec{k}'; \vec{p}) = v(\vec{k}, \vec{k}') \left[ 1 - \frac{p^2}{8\sqrt{\vec{k}^2 + m^2}\sqrt{\vec{k}'^2 + m^2}} \right]. \quad (6)$$

A relativistic potential $v$ is generated from the nonrelativistic CD Bonn $NN$ force by performing the scale transformation of Ref. [64]. This scale transformation provides phase equivalent, nonrelativistic and relativistic potentials which generate $t$ matrices obeying Lippmann-Schwinger type equations with nonrelativistic and relativistic propagators, respectively.

To describe the configuration of three nucleons we use, instead of standard Jacobi momenta [50], the relative momentum $\vec{k}$ of nucleons 2–3 in their $2N$ c.m. subsystem and momentum $\vec{q}$ of the spectator nucleon 1 in the $3N$ c.m. system. In this system, the sum of the momenta of the individual nucleons is zero, and thus $\vec{p} = -\vec{q}$ is the total momentum of the two-body subsystem responsible for the boost of this subsystem. In the nonrelativistic limit,the momentum $\vec{k}$ reduces to the standard Jacobi momentum.

In the relativistic calculations including the approximate potential of Eq. (6), it is important to check the applicability of such approximations. We checked this by calculating the deuteron wave function $\phi_d(\vec{k})$ when the deuteron is moving with momentum $\vec{p}$. In Ref. [65], we calculated the binding energy $E_d$ and $D$-state probability of the deuteron in motion as a function of laboratory energy of the incoming neutron. The results are obtained using the approximation of Eq. (6) and two additional approximations [65]. In one of them, the boost effects are neglected completely such that

$$V(k, k'; p) = v(k, k'), \quad (7)$$

and in the other, only the leading term of $p/m$ is kept in the expansion of $V(k, k'; p)$ as

$$V(k, k'; p) = v(k, k') \left[ 1 - \frac{p^2}{8m^2} \right]. \quad (8)$$

When boost effects are properly taken into account, the results must provide the deuteron binding energy and $D$-state probability approximately equal to the values for the deuteron at rest. The approximation in Eq. (6) approaches very closely the exact result even at large boosts. The complete neglect of boost [Eq. (7)] or restriction to only the $p/m$ leading term [Eq. (8)] yield poor approximations.

Presently we solve Lippmann-Schwinger type equations numerically with partial-wave decomposition. When effects of the boost on spins are included, a construction of the partial-wave states is performed with the total spin $s$ of the $2N$ subsystem defined in its c.m. system. This leads to Wigner spin rotations [65,66]. The solution of $3N$ relativistic Faddeev equations with Wigner spin rotations taken into account is very time consuming. We found in $j < 2$ calculations that the changes of the cross section due to Wigner spin rotations are smaller than 1%. For the analyzing power, these changes are slightly larger, but they do not exceed 3%, with the exception of zero crossing angle regions. Thus when performing the fully converged calculation ($j < 6$, $J \leqslant 25/2$), we neglected Wigner spin rotations completely.

## V. RESULTS AND DISCUSSION

In this section, the experimental results for the differential cross sections and vector analyzing powers are compared with their respective theoretical predictions. They were extracted from the yields of the $nd$ and $np$ elastic scattering obtained and discussed in Secs. II and III.

### A. Differential cross section

The absolute values of the $nd$ elastic scattering cross sections were deduced by normalizing the data to the $np$ scattering cross sections as given by the $NN$ phase shift analysis program SAID [67].

For the backward angle region, the differential cross sections measured at the $(n, p)$ facility were deduced as

$$\left.\frac{d\sigma}{d\Omega}\right|_{nd:\text{c.m.}} = \left.\frac{d\sigma}{d\Omega}\right|_{np:\text{c.m.}} \frac{Y_{nd}}{Y_{np}} \frac{J_{nd}}{J_{np}} \times \left( \frac{N^{\text{eff}}_{\text{target}:nd}\, \epsilon_{\text{MWDC}:nd} \epsilon_{\text{VDC}:nd}\, I_{nd}}{N^{\text{eff}}_{\text{target}:np}\, \epsilon_{\text{MWDC}:np} \epsilon_{\text{VDC}:np}\, I_{np}} \right)^{-1}, \quad (9)$$

where $d\sigma/d\Omega_{np}$ are $np$ differential cross sections obtained from the SP03 phase-shift solution of Arndt [67], $Y$ is the number of events, $J$ is the Jacobian, $N^{\text{eff}}_{\text{target}}$ is the effective target thickness, $I$ is the total number of incident neutrons, and $\epsilon$ is the efficiency of the detectors. The $np$ differential cross section $d\sigma/d\Omega_{np}$ changes slightly depending on which of the $NN$ models is used in the phase shift analysis. This results in a systematic error of up to ±3%.

We assumed that the detector solid angle in the laboratory system $\Delta\Omega(\theta)_{\text{lab}}$ is the same for the $nd$ and $np$ experiments and does not appear in Eq. (9) due to cancellation. This assumption causes a systematic uncertainty of up to ±5%. The yields $Y_{nd}, Y_{np}$ and the target thicknesses have systematic errors of ±8%, ±6%, and ±2%, respectively. The total systematic uncertainty of the cross sections is estimated to be about ±11%.

Cross sections are plotted in Fig. 5 as solid circles, and their numerical values together with statistical errors are given in Table I. These statistical errors range from 3% to 8%. Some data points obtained at identical angles in the different runs are consistent within statistical errors.

For the forward angle region, the $nd$ differential cross sections measured at the NTOF facility were deduced as

$$\left.\frac{d\sigma}{d\Omega}\right|_{nd:\text{c.m.}} = \left.\frac{d\sigma}{d\Omega}\right|_{np:\text{c.m.}} \frac{Y_{nd}}{Y_{np}} \frac{J_{nd}}{J_{np}} \left( \frac{N^{\text{eff}}_{\text{target}:nd}\, I_{nd}}{N^{\text{eff}}_{\text{target}:np}\, I_{np}} \right)^{-1}. \quad (10)$$

TABLE I. Cross section for *nd* elastic scattering at 248 MeV obtained at the $(n, p)$ facility in 2003 (upper rows) and 2000 (lower rows). Only statistical errors are given.

| $\theta_{\mathrm{c.m.}}$(deg) | $(d\sigma/d\Omega)$(mb/sr) | $\Delta(d\sigma/d\Omega)$(mb/sr) |
|---|---|---|
| 63.5 | 0.310 | 0.014 |
| 66.5 | 0.287 | 0.013 |
| 67.0 | 0.251 | 0.016 |
| 70.5 | 0.209 | 0.008 |
| 74.5 | 0.157 | 0.008 |
| 75.5 | 0.135 | 0.008 |
| 79.5 | 0.115 | 0.006 |
| 83.5 | 0.115 | 0.008 |
| 84.5 | 0.112 | 0.008 |
| 88.5 | 0.091 | 0.006 |
| 92.5 | 0.076 | 0.006 |
| 169.5 | 0.249 | 0.007 |
| 174.0 | 0.272 | 0.010 |
| 84.5 | 0.097 | 0.005 |
| 88.5 | 0.094 | 0.004 |
| 92.5 | 0.079 | 0.005 |
| 94.5 | 0.076 | 0.006 |
| 98.5 | 0.072 | 0.004 |
| 104.5 | 0.073 | 0.005 |
| 118.5 | 0.072 | 0.003 |
| 122.5 | 0.080 | 0.004 |
| 135.0 | 0.102 | 0.005 |
| 139.0 | 0.119 | 0.005 |
| 145.0 | 0.133 | 0.005 |
| 149.0 | 0.154 | 0.005 |
| 155.5 | 0.184 | 0.007 |
| 159.5 | 0.199 | 0.007 |
| 163.5 | 0.223 | 0.011 |
| 169.5 | 0.256 | 0.009 |
| 174.0 | 0.276 | 0.014 |
| 178.0 | 0.289 | 0.013 |

They are plotted in Fig. 5 as solid squares, and their numerical values are given in Table II. The statistical errors range from 5% to 9% except for the data of $\theta_{\mathrm{c.m.}} = 60^\circ$ which have an error of $\pm 25\%$. The systematic errors of $Y_{nd}$, $Y_{np}$, $\frac{d\sigma}{d\Omega}_{np:\mathrm{c.m.}}$, and $N_{\mathrm{target}}^{\mathrm{eff}}$ are $\pm 8\%$, $\pm 6\%$, $\pm 6\%$, and $\pm 8\%$, respectively. From these values, the total systematic uncertainty of the present data is estimated to be $\pm 15\%$.

TABLE II. Cross section for *nd* elastic scattering at 248 MeV obtained at the NTOF facility. Only statistical errors are given.

| $\theta_{\mathrm{c.m.}}$(deg) | $(d\sigma/d\Omega)$(mb/sr) | $\Delta(d\sigma/d\Omega)$(mb/sr) |
|---|---|---|
| 11.1 | 11.15 | 0.78 |
| 20.6 | 6.18 | 0.33 |
| 29.9 | 2.68 | 0.16 |
| 39.2 | 1.64 | 0.14 |
| 58.6 | 0.81 | 0.20 |

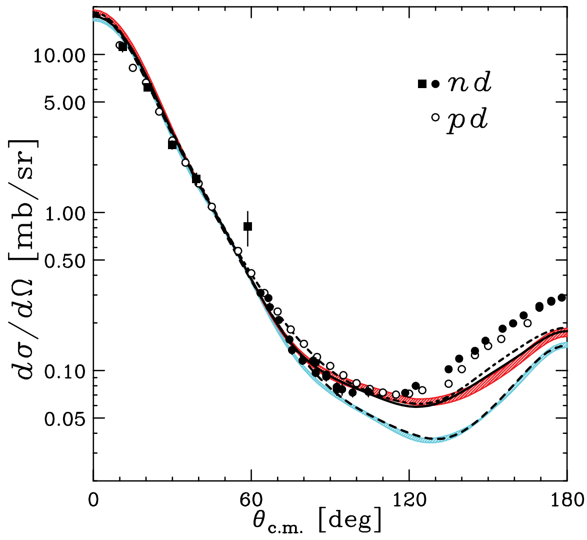

FIG. 5. (Color online) Differential cross section for *Nd* elastic scattering at 250 MeV. Solid circles and solid squares represent *nd* elastic scattering cross sections at 248 MeV obtained with the $(n, p)$ and the NTOF facility, respectively. Error bars represent only statistical errors. Open circles are data for *pd* elastic scattering [27]. Light shaded (blue) band contains predictions of realistic *NN* potentials: AV18, CD Bonn, Nijmegen I and II. Dark shaded (red) band shows results of combining these potentials with the TM99 3NF. Solid line is a prediction obtained with the AV18 + Urbana IX combination. Dot-dashed and dashed lines are predictions based on CD Bonn + $\Delta$ and CD Bonn potentials as described in Sec. IV B, respectively.

The *nd* cross sections are compared in Fig. 5 with different theoretical predictions and with the elastic *pd* scattering cross sections of Ref. [27]. The predictions with various *NN* forces are very close to each other, as shown with a narrow light shaded band. This reflects a weak dependence of the cross section on the set of *NN* potentials used in these calculations. The predictions with *NN* forces clearly underestimate the data for c.m. angles $\theta_{\mathrm{c.m.}} > 90^\circ$. Especially large differences up to about 70% exist in the region of the cross section minimum around $\theta_{\mathrm{c.m.}} = 130^\circ$. The dark shaded band shows the predictions for various combinations of *NN* force with the TM99 3NF, and the solid line shows the AV18 prediction when combined with the Urbana IX 3NF. The inclusion of the TM99 or Urbana IX 3NFs leads to a better description of the data. However, even when they are included, the theory significantly underestimates the data for $\theta_{\mathrm{c.m.}} > 120^\circ$. This is in contrast to the 135 MeV/*A* results [18], where predictions of the realistic *NN* interactions combined with the TM99 or Urbana IX 3NF described the data well over the whole angular region with the exception of forward angles $\theta_{\mathrm{c.m.}} < 40^\circ$.

It is possible that one of the origins of the remaining discrepancy between data and theory can be the lack of contributions of other than the $2\pi$ exchange components of 3NFs to the potential energy of three nucleons. The 3NFs caused by heavy meson exchanges are considered to have a shorter range than the $2\pi$-exchange 3NFs. In general, contributions of short-range interactions become larger at higher energy. As a consequence, inclusion of $\pi$-$\rho$ or $\rho$-$\rho$ exchange type 3NFs is a plausible possibility for removal of the discrepancy between the data and the theory containing only $2\pi$-exchange 3NFs. An effective 3NF due to $\pi$-$\rho$ and $\rho$-$\rho$ exchange with intermediate $\Delta$-isobar excitation is taken into account in the calculations based on the CD Bonn + $\Delta$ potential as discussed in Sec. IV B. The results are shown in Fig. 5 as dot-dashed ($NN$ + 3NF) and as dashed ($NN$ only) lines. It is seen that the prediction with $\Delta$-isobar excitation is similar to the results obtained with the TM99 or Urbana IX 3NF. Thus, the coupled-channel approach is also unable to improve the agreement between the theoretical predictions and the data. The effect of an explicit inclusion of the $\pi$-$\rho$ exchange TM 3NF [68] has yet to be checked.

Recently, calculations inclusive of relativistic effects have been done to see if they could account for the discrepancies at higher energies. We will discuss them in Sec. V C.

In Fig. 5, the open circles show the results of the $pd$ elastic scattering at 250 MeV measured at RCNP [27]. We can see some differences between the data and the theory which will be discussed in Sec. V D.

TABLE III. Nucleon vector analyzing power of $nd$ elastic scattering at 248 MeV obtained at the $(n, p)$ facility in 2003 (upper rows) and 2000 (lower rows). Only statistical errors are given.

| $\theta_{\text{c.m.}}$(deg) | $A_y$ | $\Delta A_y$ |
|---|---|---|
| 63.5 | −0.28 | 0.15 |
| 79.5 | −0.44 | 0.14 |
| 88.5 | −0.55 | 0.18 |
| 169.5 | 0.032 | 0.060 |
| 86.5 | −0.44 | 0.12 |
| 98.5 | −0.18 | 0.18 |
| 118.5 | −0.090 | 0.12 |
| 139.0 | 0.12 | 0.11 |
| 149.0 | 0.15 | 0.11 |
| 159.5 | 0.17 | 0.11 |
| 169.5 | 0.11 | 0.12 |
| 176.0 | −0.040 | 0.10 |

### B. Vector analyzing power

The experimental results for analyzing powers are shown in Fig. 6 by solid squares and solid circles. The numerical values are given in Tables III and IV. The systematic uncertainty of the analyzing powers is estimated to be about ±18%, mainly due to the systematic uncertainty of the polarization transfer coefficient $D_{NN}$ in the neutron production reaction. Because statistical errors in the analyzing powers are large in magnitude, it is difficult to draw any definite conclusions about the effects of 3NFs by comparing present data to the theoretical predictions. In the figure, $pd$ elastic scattering data [27] are represented by open circles. The data for $nd$ and $pd$ scattering are consistent with each other within statistical errors. We can see that the calculations fail to reproduce the data in the angular region $\theta_{\text{c.m.}} = 110°–140°$. The experimental data change sign at about 120°, while in the calculation this happens at around 140°. Our results show that the inclusion of 3NFs in the calculations does not improve the description of the data, as was the case for the proton analyzing powers measured at 200 MeV at Indiana University Cyclotron Facility (IUCF) [24].

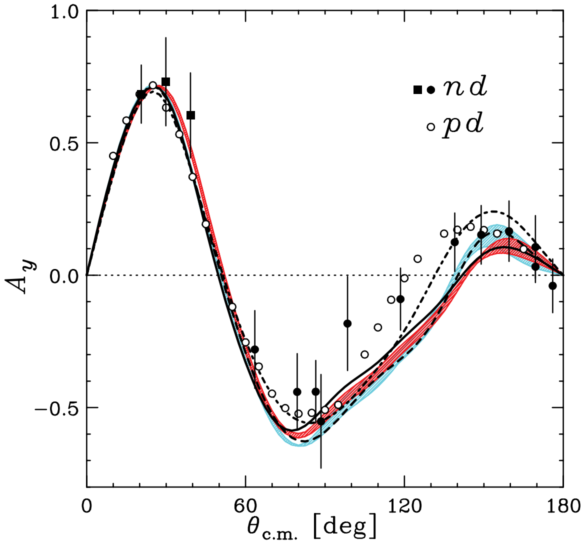

FIG. 6. (Color online ) Nucleon vector analyzing powers in $Nd$ elastic scattering at 250 MeV. For the description of data and theoretical curves, see Fig. 5. Error bars represent statistical errors only.

### C. Relativistic effects

Since inclusion of current 3NFs fails to explain the discrepancy between pure $2N$ force predictions and cross section data, it might be instructive to estimate the magnitude of relativistic effects at this energy. In Figs. 7 and 8, we show the theoretical predictions including the relativistic corrections as described in Sec. IV C. The dashed, dotted, and dash-dotted lines represent the results corresponding to the approximation given by Eqs. (6), (8), and (7), respectively. In the differential cross section, only the result with poor approximation (dash-dotted line) shows a significant deviation from the nonrelativistic result. The relatively large (10–27%) effect introduced by inclusion of relativistic potentials is restricted to the backward angle region ($\theta_{\text{c.m.}} \geqslant 160°$). In the region of the cross section minimum around $\theta_{\text{c.m.}} = 130°$, relativistic effects increase

TABLE IV. Vector analyzing power of $nd$ elastic scattering at 248 MeV obtained at the NTOF facility. Only statistical errors are given.

| $\theta_{\text{c.m.}}$(deg) | $A_y$ | $\Delta A_y$ |
|---|---|---|
| 20.6 | 0.68 | −0.11 |
| 29.9 | 0.73 | −0.17 |
| 39.2 | 0.60 | −0.16 |

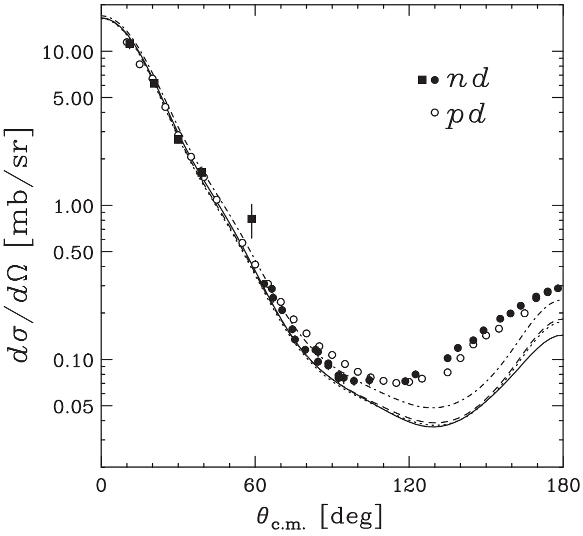

FIG. 7. Differential cross sections for *Nd* elastic scattering at 250 MeV. Solid line is the result of nonrelativistic Faddeev calculation with CD Bonn potential. Relativistic predictions which include the approximations of Eqs. (6), (8), and (7) are shown by the dashed, dotted, and dash-dotted lines, respectively. For explanation of data points, see Fig.5.

the cross section by no more than 7%. The relativistic effects would be unable to improve drastically the agreement between the data and the calculations including 3NFs.

In Ref. [30], the corrections to the *nd* total cross section resulting from relativistic kinematics were found to increase with energy and were comparable in size to 3NF effects. In a similar way, at 250 MeV the relativistic phase-space factor for the elastic scattering is estimated to be 18% larger than the nonrelativistic one. The magnitude of relativistic effects in the cross section are relatively small, because the relativistic phase-space factor increases while dynamical effects work in opposite directions. As can be seen in Fig. 7, the boost effects in the potential matrix element work in opposition to the kinematical effects, restricting relativistic effects to the backward angle region only.

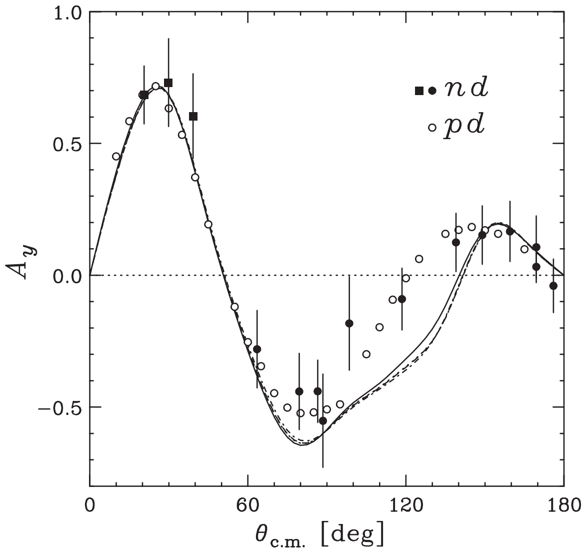

FIG. 8. Nucleon vector analyzing powers $A_y$ for *Nd* elastic scattering at 250 MeV. For the description of data and curves, see Fig. 7.

Contributions from the relativistic effects upon the analyzing power are restricted to the angular range $\theta_{\text{c.m.}} = 100^\circ$–$150^\circ$, and they shift the relativistic theory away from the data as shown in Fig. 8.

### D. Comparison of *pd* and *nd* cross sections

Although very important, the question of the magnitude of the charge asymmetry effects in the 3*N* continuum is, up to now, only partly resolved. The most important contribution to the charge asymmetry is from the *pp* Coulomb interaction. From a theoretical standpoint, accurate calculations using various configuration-space techniques [31–33,69] have been performed to include the Coulomb force for the 3*N* bound state and for the elastic *pd* scattering below and above [34] the deuteron breakup threshold. However, only recently were the calculations of *pd* scattering at intermediate energies including Coulomb forces performed via the screening and renormalization approach in the momentum-space framework [35]. The results of theoretical calculations with CD Bonn + Δ potential reproduced very well the differential cross section data for the *dp* elastic scattering at 135 MeV/*A*. At this energy, the Coulomb effect is shown to be confined to the forward angles, $\theta_{\text{c.m.}} \leqslant 30^\circ$.

Experimentally, the only way to find out the importance of the *pp* Coulomb force is by directly comparing *pd* and *nd* data. In Ref. [27], the measurement of accurate cross section data, which have systematic errors of 4% and statistical errors less than 1.4%, is reported for *pd* elastic scattering at 250 MeV over a wide angular region. This allows us to directly compare the *nd* and *pd* cross section data. To deduce the experimental *pd* values at the angles corresponding the *nd* data points, we use the cubic spline interpolation method. The ratio of the measured *pd* to *nd* cross sections is shown in Fig. 9 (solid circles). The experimental results include systematic errors which, as shown in the lower panel of Fig. 9, depend upon the scattering angle. At some backward angles, the data show significant deviations from unity.

The curves in Fig. 9 are the theoretical predictions for the *pd*/*nd* ratio at 250 MeV obtained with the CD Bonn and CD Bonn + Δ potentials. In the upper panel, three curves represent the predictions obtained when the Coulomb force is included in an approximate way using the approach of Ref. [70]. The solid and dotted lines show the predictions calculated by the Lisbon-Hannover group with and without Δ-isobar excitation, respectively. The dot-dashed curve shows the CD Bonn prediction calculated by Kamada [71]. Here, the amplitude for the *pd* elastic scattering was taken as a sum of the Rutherford amplitude and the Coulomb distorted nuclear amplitude $T_{pd}^{\text{CN}}$, obtained from the pure nuclear *nd* scattering amplitude $T_{nd}$ with the following Coulomb modification

$$\langle l|T_{pd}^{\text{CN}}|l'\rangle \approx e^{i\sigma_l}\langle l|T_{nd}|l'\rangle e^{i\sigma_{l'}}, \tag{11}$$

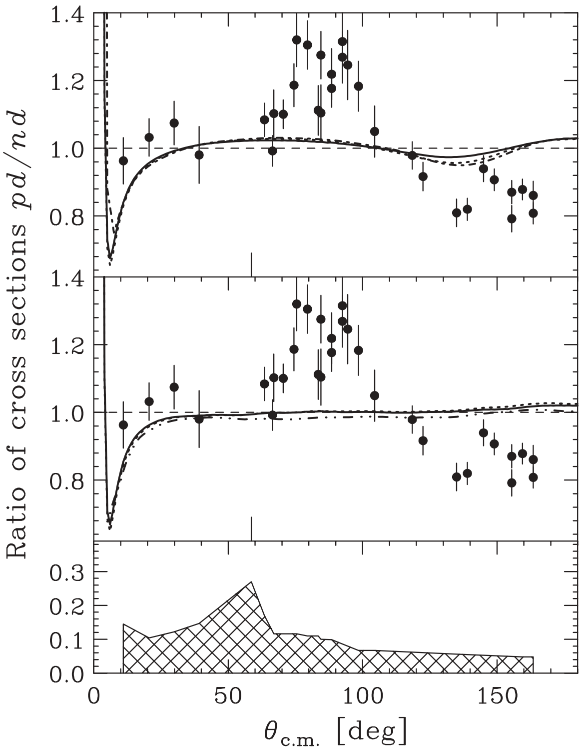

FIG. 9. Angular dependence of ratio between the *pd* and *nd* elastic scattering cross sections. Circles show the results deduced from the *nd* and *pd* data of Ref. [27] with statistical errors only. Hatched area in the lower panel shows systematic errors. Curves show theoretical predictions obtained by including the Coulomb effects in *pd* calculations. Predictions in the upper panel include the Coulomb effect by the Doleschall approximation. Those in the middle panel include the Coulomb effect by the screening and renormalization approach. Solid and dotted lines represent the predictions based on the CD Bonn + $\Delta$ and CD Bonn potentials, respectively [35]. Dot-dashed line represents the prediction based on the CD Bonn potential [71]. Dot-dot-dashed line represents the prediction taking into account the 2 MeV energy difference between *pd* and *nd*.

where $\sigma_l$ and $\sigma_{l'}$ are the Coulomb phases, and $l$ and $l'$ are the angular momenta of the $p$-$d$ two-body system in the final and initial state, respectively. The dotted and dot-dashed lines, which include CD Bonn and are calculated by different groups, are almost identical.

As can be seen in the upper panel of Fig. 9, an oscillating structure is present in the predictions. The angle where the experimental value crosses unity is around $\theta_{\text{c.m.}} = 110^\circ$, which is reproduced by the predictions that correspond to an approximate treatment of Coulomb effects.

The middle panel displays the cross section ratio, including the Coulomb interaction calculated by the screening and renormalization approach [35]. These calculations do not exhibit the oscillating structure shown by the calculations in the top panel. The deviations from unity for the theoretical ratio do not exceed 5% for the region of $\theta_{\text{c.m.}} \geqslant 30^\circ$. Regarding the $\Delta$-isobar excitation effect, we can see that the difference between the solid and dotted lines in this panel becomes smaller than that in the upper panel. The prediction for the ratio of the *pd* differential cross section at 250 MeV to the *nd* differential cross section at 248 MeV, based upon the CD Bonn potential [35] is shown as the dot-dot-dashed line in the middle panel. Compared to the dotted line, the dot-dot-dashed line is shifted down by about 2%. Except at the angles around 130°, calculations based upon these potentials predict the data within the sum of statistic and systematic errors. More precise data are soon to be measured in order to directly study Coulomb effects.

## VI. CONCLUSIONS AND SUMMARY

We performed measurements of the cross section and neutron analyzing power for the $d(\vec{n}, n)d$ reaction using a 248 MeV polarized neutron beam. To cover a wide angular range, $\theta_{\text{c.m.}} = 10^\circ$–$180^\circ$, we carried out two kinds of experiments at RCNP. The measurements for the backward angle region of $\theta_{\text{c.m.}} = 60^\circ$–$180^\circ$ were performed at the $(n, p)$ facility where the recoil deuterons were detected by using the magnetic spectrometer LAS. The measurements for the forward angle region of $\theta_{\text{c.m.}} = 10^\circ$–$60^\circ$ were performed at the NTOF facility where the energy spectra of the scattered neutrons were obtained by the time-of-flight method.

Comparison of measured *nd* cross sections with theories based on various *NN* potentials revealed a clear difference between pure $2N$ force predictions and the results obtained with inclusion of 3NFs. However, the large discrepancy between *nd* cross sections and *NN* force predictions for $\theta_{\text{c.m.}} \geqslant 90^\circ$ can only be partially removed by including the TM99 or Urbana IX 3NFs or an effective 3NF due to explicit $\Delta$-isobar excitation. Theoretical predictions including 3NFs still underestimate the data by up to 40%. Present-day relativistic Faddeev calculations show that relativistic effects are significant only in the region of backward angles where they increase the cross section by up to 27%. They are relatively small in the region of the differential cross section minimum around $\theta_{\text{c.m.}} = 130^\circ$ where the discrepancies between $2N$ force predictions and data are largest. This implies that the remaining discrepancy between cross section data and calculations is likely due to inadequate modeling of the $2N$ or $3N$ forces used in the present calculations. This discrepancy might be resolved by inclusion of shorter range 3NFs not mediated by $\Delta$ isobar, which in the traditional meson-exchange picture might result from $\pi$-$\rho$ exchanges between three nucleons [68].

We compare the *nd* and *pd* data directly over a wide angular region. The *nd* cross sections roughly agree with the *pd* data with a reduced $\chi^2$ of 9.7. However, a detailed comparison of *pd* and *nd* data shows a characteristic oscillating angular dependence for the *pd* to *nd* ratio. Recent calculations including the Coulomb effects underestimate the magnitude of the observed oscillation at some angles. Discrepancies between the data and the predictions may imply an isospin dependence of *NN* or 3NF potentials.

The measurements of the elastic *nd* scattering at 95 MeV at TSL Uppsala [72–74] also provide a direct comparison between the *nd* and *pd* data in the intermediate energy region. The *nd* and *pd* data agree with each other with a reduced $\chi^2$

of 2.6, but the *pd* data have large uncertainties. The energy dependence of Coulomb force effects may be studied by making use of the recently obtained data from the RCNP *pd* measurement at 100 MeV [75].

## ACKNOWLEDGMENTS

We acknowledge the outstanding work of the RCNP Accelerator group for delivering an excellent proton beam. We also thank Y. Hagihara, D. Hirooka, K. Itoh, T. Ikeda, M. Kato, Y. Kitamura, T. Kudoh, Y. Nagasue, S. Sakoda, Y. Satou, N. Uchigashima for their precious collaboration. Y. M. acknowledges the support of the research grants of the Japan Society for the Promotion of Science (JSPS) for Young Scientists. H.K. thanks Y. Koike for fruitful discussion about the Coulomb effects. H.W. thanks the University of Tokyo and RCNP for hospitality and support during his stay in both institutes. Some of the numerical calculations were performed on the IBM Regatta p690+ of the NIC in Jülich, Germany. A D. is supported by the Portuguese Fundação para a Ciência e a Tecnologia (FCT) grant SFRH/BPD/14801/2003, A.C.F. in part by the FCT grant POCTI/ISFL/2/275, and P.U.S. in part by the Deutsche Forschungsgemeinschaft grant Sa 247/25. This work was supported financially in part by the Grants-in-Aid for Scientific Research Nos. 04402004 and 10304018 of the Ministry of Education, Culture, Sports, Science, and Technology of Japan, and by the Polish Committee for Scientific Research under Grant No. 2P03B00825.

[1] R. B. Wiringa, V. G. J. Stoks, and R. Schiavilla, Phys. Rev. C **51**, 38 (1995).
[2] R. Machleidt, F. Sammarruca, and Y. Song, Phys. Rev. C **53**, R1483 (1996).
[3] V. G. J. Stoks, R. A. M. Klomp, C. P. F. Terheggen, and J. J. de Swart, Phys. Rev. C **49**, 2950 (1994).
[4] A. Nogga, H. Kamada, and W. Glöckle, Phys. Rev. Lett. **85**, 944 (2000).
[5] A. Nogga, H. Kamada, W. Glöckle, and B. R. Barrett, Phys. Rev. C **65**, 054003 (2002).
[6] J. Carlson and R. Schiavilla, Rev. Mod. Phys. **70**, 743 (1998).
[7] R. B. Wiringa, S. C. Pieper, J. Carlson, and V. R. Pandharipande, Phys. Rev. C **62**, 014001 (2000).
[8] S. Coon, M. Scadron, P. McNamee, B. R. Barrett, D. Blatt, and B. McKellar, Nucl. Phys. **A317**, 242 (1979).
[9] B. S. Pudliner, V. R. Pandharipande, J. Carlson, S. C. Pieper, and R. B. Wiringa, Phys. Rev. C **56**, 1720 (1997).
[10] J. Fujita and H. Miyazawa, Prog. Theor. Phys. **17**, 360 (1957).
[11] E. Epelbaum, W. Glöckle, and U.-G. Meißner, Nucl. Phys. **A637**, 107 (1998).
[12] E. Epelbaum, W. Glöckle, and U.-G. Meißner, Nucl. Phys. **A671**, 295 (2000).
[13] E. Epelbaum, Prog. Part. Nucl. Phys. **57**, 654 (2006).
[14] H. Shimizu *et al.*, Nucl. Phys. **A382**, 242 (1982).
[15] H. Rühl *et al.*, Nucl. Phys. **A524**, 377 (1991).
[16] H. Sakai *et al.*, Phys. Rev. Lett. **84**, 5288 (2000).
[17] N. Sakamoto *et al.*, Phys. Lett. **B367**, 60 (1996).
[18] K. Sekiguchi *et al.*, Phys. Rev. C **65**, 034003 (2001).
[19] K. Sekiguchi *et al.*, Phys. Rev. Lett. **95**, 162301 (2005).
[20] K. Ermisch *et al.*, Phys. Rev. Lett. **86**, 5862 (2001).
[21] R. Bieber *et al.*, Phys. Rev. Lett. **84**, 606 (2000).
[22] H. Witała *et al.*, Few-Body Syst. **15**, 67 (1993).
[23] J. Arvieux *et al.*, Phys. Rev. Lett. **50**, 19 (1983).
[24] E. J. Stephenson, H. Witała, W. Glöckle, H. Kamada, and A. Nogga, Phys. Rev. C **60**, 061001(R) (1999).
[25] R. V. Cadman *et al.*, Phys. Rev. Lett. **86**, 967 (2001).
[26] K. Sekiguchi *et al.*, Phys. Rev. C **70**, 014001 (2004).
[27] K. Hatanaka *et al.*, Phys. Rev. C **66**, 044002 (2002).
[28] H. Witała, W. Glöckle, D. Hüber, J. Golak, and H. Kamada, Phys. Rev. Lett. **81**, 1183 (1998).
[29] W. P. Abfalterer *et al.*, Phys. Rev. Lett. **81**, 57 (1998).
[30] H. Witała, H. Kamada, A. Nogga, W. Glöckle, C. Elster, and D. Hüber, Phys. Rev. C **59**, 03035 (1999).
[31] A. Kievsky, M. Viviani, and S. Rosati, Phys. Rev. C **52**, R15 (1995).
[32] A. Kievsky, Nucl. Phys. **A607**, 402 (1996).
[33] A. Kievsky, Phys. Rev. C **60**, 034001 (1999).
[34] A. Kievsky, M. Viviani, and S. Rosati, Phys. Rev. C **64**, 024002 (2001).
[35] A. Deltuva, A. C. Fonseca, and P. U. Sauer, Phys. Rev. C **71**, 054005 (2005).
[36] A. Deltuva, A. C. Fonseca, A. Kievsky, S. Rosati, P. U. Sauer, and M. Viviani, Phys. Rev. C **71**, 064003 (2005).
[37] K. Yako *et al.*, Nucl. Phys. **A684**, 563c (2001).
[38] K. Hatanaka *et al.*, Nucl. Instrum. Methods A **384**, 575 (1997).
[39] T. Wakasa *et al.*, Nucl. Instrum. Methods A **482**, 79 (2002).
[40] R. A. Arndt, L. D. Roper, R. A. Bryan, R. B. Clark, B. J. VerWest, and P. Signell, Phys. Rev. D **28**, 97 (1983).
[41] J. Kamiya *et al.*, RCNP Annual Report 1998, p. 113.
[42] T. Taddeucci *et al.*, Phys. Rev. C **41**, 2548 (1990).
[43] T. Wakasa *et al.*, Phys. Rev. C **51**, R2871 (1995).
[44] R. Henderson *et al.*, Nucl. Instrum. Methods A **257**, 97 (1987).
[45] Y. Maeda *et al.*, Nucl. Instrum. Methods A **490**, 518 (2002).
[46] N. Matsuoka *et al.*, RCNP Annual Report 1987, p. 176.
[47] N. Matsuoka *et al.*, RCNP Annual Report 1991, p. 190.
[48] H. Sakai *et al.*, Nucl. Instrum. Methods A **369**, 120 (1996).
[49] T. Wakasa *et al.*, Nucl. Instrum. Methods A **404**, 355 (1998).
[50] W. Glöckle, H. Witała, D. Hüber, H. Kamada, and J. Golak, Phys. Rep. **274**, 107 (1996).
[51] D. Hüber, H. Kamada, H. Witała, and W. Glöckle, Acta Phys. Pol. B **28**, 1677 (1997).
[52] H. Witała, T. Cornelius, and W. Glöckle, Few-Body Syst. **3**, 123 (1988).
[53] D. Hüber, H. Witała, and W. Glöckle, Few-Body Syst. **14**, 171 (1993).
[54] S. A. Coon and H. K. Han, Few-Body Syst. **30**, 131 (2001).
[55] J. L. Friar, D. Hüber, and U. van Kolck, Phys. Rev. C **59**, 53 (1999).
[56] D. Hüber, J. Friar, A. Nogga, H. Witała, and U. van Kolck, Few-Body Syst. **30**, 95 (2001).
[57] A. Deltuva, K. Chmielewski, and P. U. Sauer, Phys. Rev. C **67**, 034001 (2003).
[58] R. Machleidt, Phys. Rev. C **63**, 024001 (2001).

[59] A. Deltuva, R. Machleidt, and P. U. Sauer, Phys. Rev. C **68**, 024005 (2003).

[60] E. O. Alt, P. Grassberger, and W. Sandhas, Nucl. Phys. **B2**, 167 (1967).

[61] A. Deltuva, A. C. Fonseca, and P. U. Sauer, Phys. Rev. C **72**, 054004 (2005).

[62] W. Glöckle, T.-S. H. Lee, and F. Coester, Phys. Rev. C **33**, 709 (1986).

[63] H. Kamada, W. Glöckle, J. Golak, and C. Elster, Phys. Rev. C **66**, 044010 (2002).

[64] H. Kamada and W. Glöckle, Phys. Rev. Lett. **80**, 2547 (1998).

[65] H. Witała, J. Golak, W. Glöckle, and H. Kamada, Phys. Rev. C **71**, 054001 (2005).

[66] B. D. Keister and W. N. Polyzou, Adv. Nucl. Phys. **20**, 225 (1991).

[67] R. A. Arndt and L. D. Roper, Scattering Analysis Program (SAID), Virginia Polytechnic Institute and State University (unpublished), see also Phys. Rev. C **56**, 3005 (1997), and references therein.

[68] S. A. Coon and M. T. Peña, Phys. Rev. C **48**, 2559 (1993).

[69] S. Ishikawa, M. Tanifuji, and Y. Iseri, Phys. Rev. C **67**, 061001(R) (2003).

[70] P. Doleschall, W. Gruebler, V. Koenig, P. Schmelzbach, F. Sperisen, and B. Jenny, Nucl. Phys. **A380**, 72 (1982).

[71] H. Kamada and Y. Koike in private communication. The prediction is based on the code from Ref. [52].

[72] P. Mermod *et al.*, Phys. Lett. **B597**, 243 (2004).

[73] P. Mermod *et al.*, Phys. Rev. C **72**, 061002(R) (2005).

[74] P. Mermod *et al.*, Phys. Rev. C **74**, 054002 (2006).

[75] Y. Tameshige *et al.* in private communication.